Study of structural and electrical properties of ferroelectric HZO films obtained by single-target sputtering

Mohammed-Bilal Hachemi, Bassem Salem, Vincent Consonni, Herve Roussel, A. Garraud, Gauthier Lefevre, Sébastien Labau, Skandar Basrour, Ahmad Bsiesy

▶ **To cite this version:**

Mohammed-Bilal Hachemi, Bassem Salem, Vincent Consonni, Herve Roussel, A. Garraud, et al.. Study of structural and electrical properties of ferroelectric HZO films obtained by single-target sputtering. AIP Advances, 2021, 10.1063/5.0058656 . hal-03439509

HAL Id: hal-03439509
https://hal.science/hal-03439509

Submitted on 29 Nov 2021

HAL is a multi-disciplinary open access archive for the deposit and dissemination of scientific research documents, whether they are published or not. The documents may come from teaching and research institutions in France or abroad, or from public or private research centers.

L'archive ouverte pluridisciplinaire **HAL**, est destinée au dépôt et à la diffusion de documents scientifiques de niveau recherche, publiés ou non, émanant des établissements d'enseignement et de recherche français ou étrangers, des laboratoires publics ou privés.

Distributed under a Creative Commons Attribution - NonCommercial 4.0 International License

AIP Advances

Study of structural and electrical properties of ferroelectric HZO films obtained by single-target sputtering

Cite as: AIP Advances **11**, 085004 (2021); https://doi.org/10.1063/5.0058656
Submitted: 24 June 2021 • Accepted: 15 July 2021 • Published Online: 02 August 2021

M. B. Hachemi, B. Salem, V. Consonni, et al.

View Online Export Citation CrossMark

ARTICLES YOU MAY BE INTERESTED IN

Ferroelectricity in hafnium oxide thin films
Applied Physics Letters **99**, 102903 (2011); https://doi.org/10.1063/1.3634052

Study of ferroelectric characteristics of $Hf_{0.5}Zr_{0.5}O_2$ thin films grown on sputtered or atomic-layer-deposited TiN bottom electrodes
Applied Physics Letters **117**, 022902 (2020); https://doi.org/10.1063/5.0011663

Evolution of phases and ferroelectric properties of thin $Hf_{0.5}Zr_{0.5}O_2$ films according to the thickness and annealing temperature
Applied Physics Letters **102**, 242905 (2013); https://doi.org/10.1063/1.4811483

Call For Papers!
AIP Advances
SPECIAL TOPIC: Advances in Low Dimensional and 2D Materials

AIP Publishing

© 2021 Author(s).

Study of structural and electrical properties of ferroelectric HZO films obtained by single-target sputtering

Cite as: AIP Advances 11, 085004 (2021); doi: 10.1063/5.0058656
Submitted: 24 June 2021 • Accepted: 15 July 2021 •
Published Online: 2 August 2021

View Online Export Citation CrossMark

M. B. Hachemi,[1,2] B. Salem,[1,a)] V. Consonni,[3] H. Roussel,[3] A. Garraud,[1] G. Lefevre,[1] S. Labau,[1] S. Basrour,[2] and A. Bsiesy[1,a)]

AFFILIATIONS

[1] University Grenoble Alpes, CNRS, CEA/LETI-Minatec, Grenoble INP, LTM, 38054 Grenoble, France
[2] University Grenoble Alpes, CNRS, Grenoble INP, TIMA, 38000 Grenoble, France
[3] University Grenoble Alpes, CNRS, Grenoble INP, LMGP, 38000 Grenoble, France

[a)] **Authors to whom correspondence should be addressed:** bassem.salem@cea.fr and ahmad.bsiesy@cea.fr

ABSTRACT

In this work, we study the structural and electrical properties of Hafnium Zirconium Oxide (HZO) thin films deposited by $Hf_{0.5}Zr_{0.5}O_2$ single-target sputtering to fabricate a TiN/(14-/22 nm-thick) HZO/TiN stack. The structural analysis of the HZO thin films performed by *in situ* x-ray diffraction upon thermal annealing shows the formation of the HZO orthorhombic phase at annealing temperatures as low as 370 °C. X-ray photoelectron spectroscopy interestingly reveals an identical chemical composition of the deposited HZO thin films and the sputtered target, i.e., an Hf:Zr ratio of 1:1. The current–voltage characteristic of the TiN/HZO/TiN stack shows a current density of 10^{-5} A/cm^2 at an applied electric field of 1 MV/cm, which, being rather low, gives a strong indication of the good electrical quality of the HZO layer. Finally, a butterfly-like capacitance–voltage loop is obtained on the TiN/HZO/TiN stack, indicating a ferroelectric behavior of the HZO layer.

© 2021 Author(s). All article content, except where otherwise noted, is licensed under a Creative Commons Attribution (CC BY) license (http://creativecommons.org/licenses/by/4.0/). https://doi.org/10.1063/5.0058656

I. INTRODUCTION

Owing to the increase in worldwide environmental awareness about the risk of using lead-containing (Pb) electronic devices, the replacement of lead-based materials from all the consumer items has become a global demand. In particular, this has led the scientific community to consider alternatives to the popular Pb(Zr, Ti)O_3 (PZT) alloy used for its high ferroelectric and piezoelectric properties in passive components, such as ferroelectric capacitors[1] or in MEMS sensors or actuator devices.[2,3] However, the replacement of PZT still remains a big challenge. Indeed, many materials have been suggested as lead-free alternatives, such as KNN,[4] $LiNbO_3$,[5] and others.[6] Nevertheless, due to the common drawbacks of these materials, including the partial CMOS compatibility, volatility, or limited functional thickness, a new class of lead-free materials based on hafnium thin films has garnered important interest after the discovery of Si-doped HfO_2 ferroelectric properties in 2011.[7] Thanks to this material's CMOS compatibility, nontoxicity, and well-known properties, this discovery has opened new perspectives toward ferroelectric devices in both CMOS and MEMS technology.

Successful integration of doped-HfO_2 ferroelectric thin films in devices such as ferroelectric memories,[8–10] ferroelectric transistors,[8,11] and ferroelectric tunnel junctions[12,13] has since been demonstrated.

Many dopants have been used to demonstrate doped-HfO_2 ferroelectric properties (La, Y, Gd, Sr, Zr, etc.).[14–18] Among them, zirconium (Zr) is one of the HfO_2 dopants with the particularity of being highly miscible with Hf due to several physical and chemical similarities between HfO_2 and ZrO_2 (e.g., the same fluorite-type structure and the same electronic configuration), which allows us to obtain alloys with a 1:1 Hf:Zr ratio. Hafnium Zirconium Oxide (HZO) presents numerous benefits such as lower deposition temperature[19] than Si-doped HfO_2 and stable ferroelectric behavior.[20] Atomic layer deposition (ALD) was the first deposition technique and the most used one to obtain ferroelectric HZO thin films due to self-limited surface reactions that allows very good film thickness

© Author(s) 2021

control and enables accurate film chemical composition.[18] Interesting results of ferroelectric HZO have been obtained by sputtering as well.[21–23]

The same environmental and sustainability motivation to replace PZT has led us to consider the use and development of single-target sputtering of HZO instead of ALD, the most widely used deposition technique of HZO. Indeed, the single-target sputtering technique, being cheaper than ALD and exhibiting higher throughputs, is more suitable for industrial processes. Moreover, the fabrication of HZO targets has a smaller environmental impact than the metalorganic precursors used in ALD in terms of cost, energy consumption, and process complexity.

To date, only few research teams have initiated studies on sputtered ferroelectric HfO_2-based thin films. Xu *et al.* reported ferroelectric behavior of HfO_2 film doped with various cations (Sc, Ge, Y, Zr, and Nb).[24] In 2017, Lee *et al.* published a report on the fabrication of ferroelectric HZO films deposited by reactive co-sputtering through the investigation of the role of target power and working pressure, as well as the thermal annealing conditions.[25] In the co-sputtering process, monitoring the chemical composition of HZO through the ratio of Hf:Zr is more challenging than the straightforward single-target sputtering system, as shown in the results of the study by Woo *et al.*[22] and Ryu *et al.*[21]

In the first part of this paper, we study the impact of sputtering conditions on HZO film properties in terms of stoichiometry, chemical composition, deposition rate, and the interfaces within the stack using x-ray photoelectron spectroscopy (XPS) and x-ray reflectivity (XRR) while highlighting the single-target sputtering advents. The second part of the paper is focused on two aspects: (1) the HZO structural analysis using grazing-incidence x-ray diffraction (GIXRD) in an *ex situ* manner after rapid thermal annealing (RTA) and XRD in an *in situ* manner upon thermal annealing to identify the temperature range yielding HZO crystallization in the orthorhombic phase and (2) the electrical properties of the TiN/HZO/TiN stack through current–voltage characteristics that gives access to leakage current analysis and through a capacitance–voltage loop that gives evidence of the HZO ferroelectric properties.

II. EXPERIMENTAL CONDITIONS

p-type (100) silicon substrates covered with a native SiO_2 layer were used to deposit the TiN/HZO/TiN stack. A 50 nm-tick TiN layer used as a bottom electrode was deposited by magnetron sputtering (Alliance Concept CT 100) using a Ti target under a $N_2{}^+Ar$ plasma at a pressure of $3 \cdot 10^{-3}$ mbar and 100 W magnetron power. The Ar and N_2 gas flow rates were 40 and 5 SCCM, respectively. Another sputtering chamber (Alliance Concept DP 850) was then used to deposit the HZO thin film by using a $Hf_{0.5}Zr_{0.5}O_2$ single target. The HZO films were deposited by sputtering at room temperature in a reactor with a 120 mm target–substrate distance. The process pressure was $4.5 \cdot 10^{-3}$ mbar with an Ar flow rate of 60 SCCM. The power density applied to the HZO target was kept at 3.33 W cm^{-2} (400 W total input power).

After deposition, the top electrode consisting of a 50 nm-thick TiN layer was deposited under the same conditions as the bottom TiN electrode. The TiN/HZO/TiN stack was exposed to rapid thermal annealing (RTA) (Jetfirst100, Jipelec). A 50 nm-thick Ti layer and 200 nm-thick Au layer were then evaporated (MEB550, PLASSYS) on top of the stack. The whole stack was patterned by an SUSS MicroTec MJB4 mask aligner using a standard AZ5214 photoresist and etched-back by reactive ion etching in an inductively coupled plasma (ICP) reactor with Cl_2, Ar, and N_2 gases (PlasmaLab100 from Oxford). Current–voltage (I–V) and capacitance–voltage (C–V) characteristics were determined using a Keithley 4200A SCS analyzer. Capacitance was measured at a frequency of 10 kHz. The dielectric constant was extracted from the C–V measurements.

X-ray photoelectron spectroscopy (XPS) was performed using a Thermo Fisher Scientific Theta 300 with a monochromatic Al K_α source, a beam size of 400 μm, and a pass energy of 100 eV. XPS was used to determine the stoichiometry and chemical state of the elements in the HZO films. XRR measurements were collected to determine the thickness, roughness, and density of HZO films, while GIXRD and conventional XRD measurements were recorded to investigate its crystalline structure and orientation. XRR scanning was performed using a Bruker D8 Advance diffractometer with Cu $K_{\alpha 1}$ radiation. GIXRD acquisitions were collected with a RIGAKU Smartlab diffractometer equipped with a 9 kW rotating anode Cu source (45 kV and 200 mA). Detector scanning was performed in the range of 25°–40° (in 2-theta scale) with a step size of 0.06° and a speed equal to 0.03°/min. The omega incidence was set to 0.45°. XRD patterns were collected with the same RIGAKU Smartlab diffractometer using the Bragg–Brentano configuration. A Ni K_β filter was set to obtain the Cu radiation (lambda was the Kα average of copper = 0.1544 nm). The θ–2θ XRD measurements were performed in the range of 25°–35° (in 2-theta scale) with a step size of 0.008° and a speed equal to 1°/min. The Anton Paar DHS1100 heating stage was used under a nitrogen atmosphere, where the samples were held by two metal clips and the chamber was closed by a hemispherical graphite dome cooled by compressed air above 200 °C. The temperature was varied from room temperature up to 900 °C. XRD scanning was carried out at room temperature (30 °C), then at 50 °C, every 25 °C up to 900 °C, and every 25 °C down to 50 °C. The thickness of the films was measured also by FIB SEM (Focused Ion Beam Scanning Electron Microscopy). The roughness of the films was also analyzed by atomic force microscopy (AFM) on a Bruker Dimension ICON system in the tapping mode using VTESPA-300 probes.

III. RESULTS AND DISCUSSION

A. Chemical composition of HZO thin films

The HZO layer chemical composition was studied by XPS, which can also yield the chemical bond nature through the analysis of the XPS peak chemical shift. By varying the x-ray beam incident angle between 23° and 73°, the HZO layer was probed to a depth of 10 nm. The XPS core level of Hf_{4f}, Zr_{3d}, O_{1s}, and C_{1s} peaks recorded is shown in Figs. 1(a)–1(d) for HZO 14 and 22 nm thick films. The different XPS peaks were positioned, and the corresponding elements were identified by taking the C_{1s} peak as a reference. The small shift in energy is between the C_{1s} peak for the two samples while the other elements are equally separated from the C_{1s} peak.

© Author(s) 2021

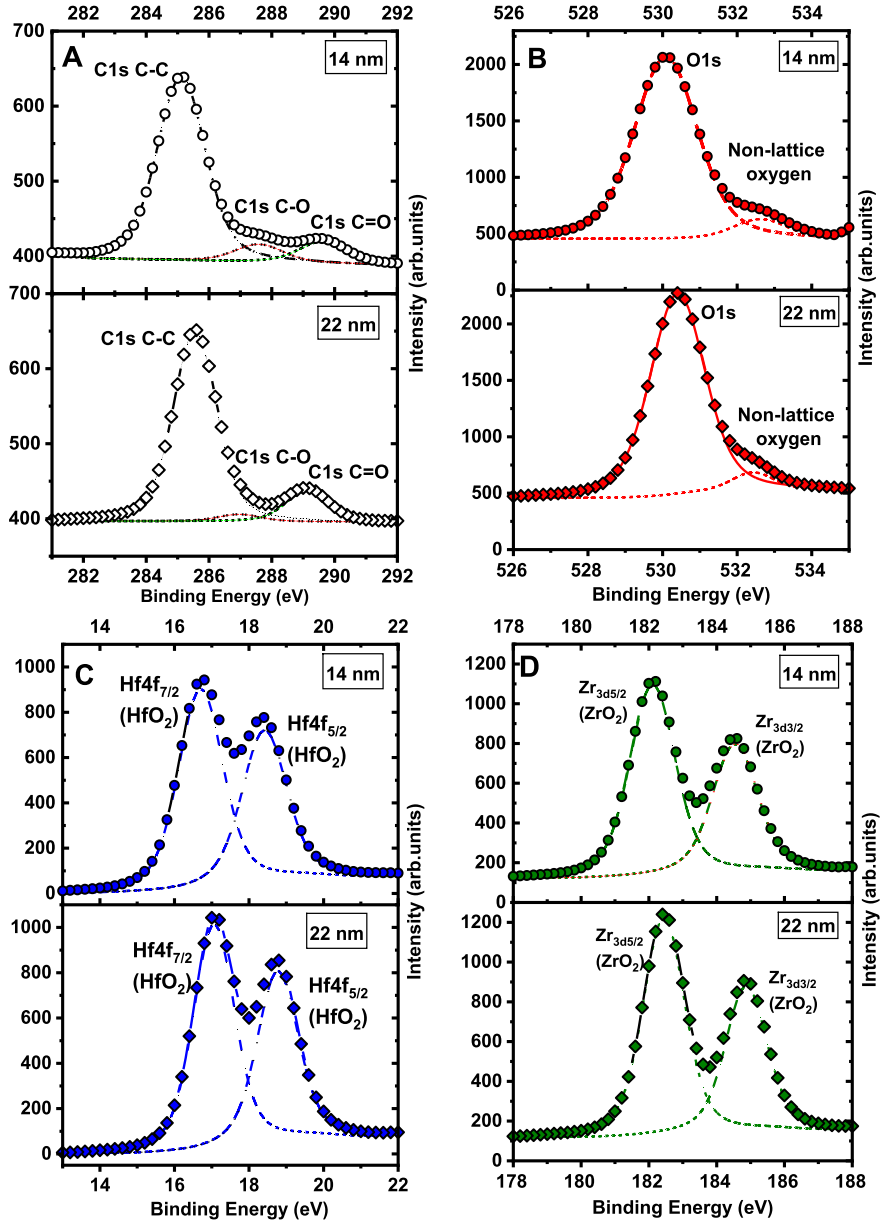

FIG. 1. XPS spectra of HZO layers (14 or 22 nm) recorded in four binding energy regions corresponding to different chemical elements: (a) C_{1s}, (b) O_{1s}, (c) Hf_{4f}, and (d) Zr_{3d} XPS. The spectra were recorded with a takeoff angle of 23.75°.

For both samples, the Hf, Zr, and O elements are equally distant from the C_{1s} peak. In Fig. 1(c), two components are identified at 16.3 and 17.9 eV corresponding to hafnium oxide O–Hf–O bonds. Moreover, the $Hf_{4f5/2}/Hf_{4f7/2}$ doublet spin-orbit splitting and the peak intensity ratio are 1.6 eV and ~3/4, respectively, in good agreement with reported values.[26] Similarly, the Zr_{3d} spectrum consists of two spin-orbit splitted peaks at 181.8 and 184.1 eV as illustrated in Fig. 1(d). The energy splitting of 2.4 eV and the $Zr_{3d3/2}/Zr_{3d5/2}$ intensity ratio of are consistent with ZrO_2 values found in the literature.[27] The C_{1s} spectrum depicted in Fig. 1(a) was decomposed into three contributions, namely, C–C, C–O, and C=O, arising from typical ambient carbon contamination. The O_{1s} peak presented in Fig. 1(b) consists of two very close peaks; the Hf–O and Zr–O bonds and the O–Hf–O and O–Zr–O bonds overlapped at 529.69–530 eV. The O–O bond observed at 532.12 eV corresponds to interstitial oxygen related to Hf and Zr sub-oxides.

Figure 2 shows the evolution of the deposition rate as a function of the increasing power density applied to the target. This high deposition rate along with the conservation of the target chemical composition in the deposited layer represents a strong advent of using a HZO single-target. The ratio was extracted from the XPS spectra similar to those shown in Fig. 1. The HZO single target used in this work has a Hf:Zr ratio of 1:1. It confirms that the deposited

© Author(s) 2021

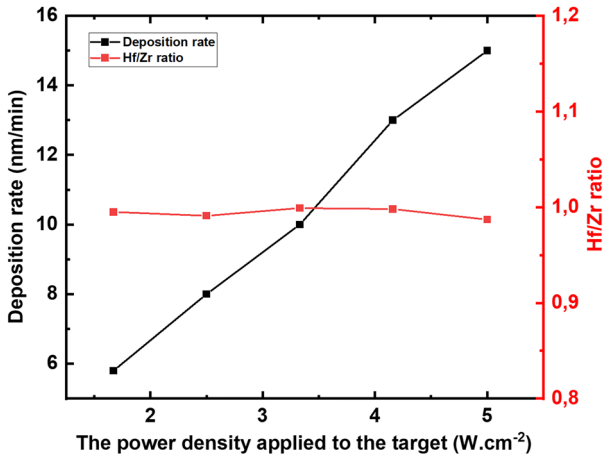

FIG. 2. HZO film deposition rate vs target power density of the single-target sputtering and the Hf:Zr ratio vs target power density as extracted from XPS spectra.

film has the same chemical composition as the sputtered target for a power density ranging from ~1 to 5 W cm^{-2} although the deposition rate increases as well as the evolution of the Hf:Zr ratio in HZO films.

B. Crystallographic structure of HZO

1. Rapid thermal annealing

As previously mentioned, the ferroelectric behavior of HZO originates from the stabilization of its orthorhombic (non-centrosymmetric) crystalline phase, which is generally obtained by crystallizing as-deposited amorphous HZO by rapid thermal annealing.[7] In this section, the effect of rapid thermal annealing on the structural properties of HZO films was studied by GIXRD measurements. Figure 3(a) shows the GIXRD data for the as-deposited and thermally processed 14 nm-thick HZO films at different temperatures. The as-deposited film shows no clear GIXRD peak, suggesting that the film is amorphous, which represents the ideal starting point toward inducing ferroelectricity following the subsequent rapid thermal annealing.[7] Moreover, the occurrence of three diffraction peaks upon thermal annealing is revealed, indicating progressive HZO film crystallization. Indeed, the GIXRD patterns show a major contribution from the orthorhombic/tetragonal phases with a predominant broad diffraction peak around 2θ = 30.4°, corresponding to the (011) and (111) reflections of the Pb_{c21} orthorhombic and P_{42nmc} tetragonal phases, respectively. A diffraction peak with a smaller intensity also occurs around 2θ = 51°, corresponding to the (220) reflection of the Pb_{c21} orthorhombic phase. The third diffraction peak observed at 2θ = 28.6° is attributed the P_{21c} monoclinic phase through the (−111) reflection. All three diffraction peaks appear at an annealing temperature of 500 °C, then increase steadily in intensity up to 600 °C, and starts to slightly decrease at 650 °C. These results show that the orthorhombic/tetragonal phases can readily be obtained by the crystallization of an amorphous as-deposited HZO film. Although the monoclinic phase is also formed, the orthorhombic/tetragonal

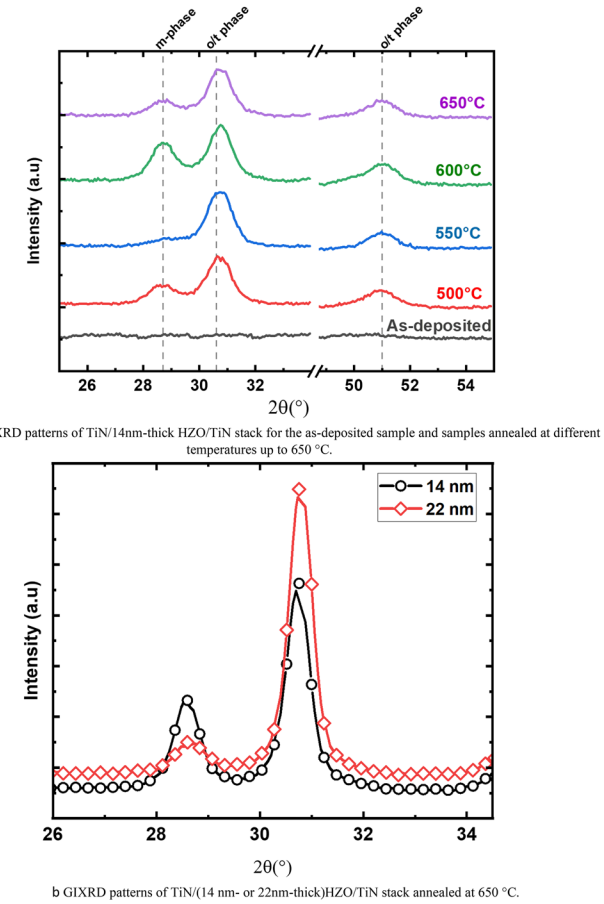

FIG. 3. (a) GIXRD patterns of the TiN/14nm-thick HZO/TiN stack for the as-deposited sample and samples annealed at different temperatures up to 650 °C. (b) GIXRD patterns of the TiN/(14- or 22 nm-thick) HZO/TiN stack annealed at 650 °C.

phases are expected to be predominant over the investigated range of annealing temperature. The phase distribution is, however, dependent upon the annealing temperature. Finally, it is worth mentioning that the thermal annealing duration of 60 s was selected after a result (not shown here), where no difference in the diffraction pattern was evidenced for a 30 and 120 s thermal annealing duration at 550 °C.

Figure 3(b) presents the GIXRD patterns for HZO films with two thicknesses of 14 and 22 nm, both annealed for 60 s at 650 °C under nitrogen atmosphere. For the 22 nm-thick HZO film, the as-deposited film turned to be amorphous too. It can be seen that after annealing at 650 °C, the monoclinic and orthorhombic/tetragonal HZO phases appear in the 22 nm-thick film, similar to the 14 nm-thick film. Interestingly, the relative peak intensity of the orthorhombic/tetragonal to monoclinic phases is higher in the case of the thicker film, which is confirmed by the higher dielectric constant for the thicker film (the dielectric constant of the o-phase is 40[28,29] and m-phase is 18.9[30]).

© Author(s) 2021

2. XRD analysis of the crystallization of HZO films under in situ thermal annealing

The results presented in Fig. 3 strongly suggest the formation of the HZO orthorhombic phase following rapid thermal annealing. However, the corresponding diffraction peak observed around 2θ = 30.4° might also be referred to as the tetragonal phase. In order to properly identify the respective contributions of the orthorhombic and tetragonal phases to this diffraction peak, XRD analysis was performed in an *in situ* manner by limiting the θ–2θ scans to the area of interest. The diffractometer coupled to an Anton Paar heating stage had the capability of exposing the sample to *in situ* thermal annealing from room temperature up to 900 °C under a nitrogen atmosphere while collecting an XRD pattern every 25 °C step. In this way, the diffraction angle-temperature map was designed.

Figure 4 presents the XRD patterns plotted within a 2θ-annealing temperature map for the as-deposited and annealed TiN/22 nm-thick HZO/TiN stack. The 2θ angle was limited to the 30°–33° range to focus on the evolution of the orthorhombic and tetragonal phases as a function of the annealing temperature. The as-deposited HZO film is found to be amorphous and starts to crystallize at around 370 °C. Moreover, the occurrence of two distinct diffraction peaks upon thermal annealing is revealed and is likely related to the Pb_{c21} orthorhombic phase [(011) reflection] and the P_{42nmc} tetragonal phase [(111) reflection], respectively. More precisely, Fig. 5 presents an XRD pattern extracted from Fig. 4 at an annealing temperature of 650 °C. It is shown that two well identified diffraction peaks occur at 2θ = 30.25° and at 2θ = 30.5°, which are attributed to the orthorhombic and tetragonal phases, respectively. As direct evidence of the existence of the orthorhombic phase in HZO film, this result allows us to access the monoclinic and orthorhombic/tetragonal phase co-existence that is reported as being crucial for inducing ferroelectricity in HfO_2 thin films.[31,32] This result further suggests that the diffraction peak reported in Fig. 3 around 2θ = 30.4° is the combination of two distinct peaks with a major contribution of the orthorhombic phase as compared to the tetragonal phase, which is a prerequisite to the occurrence of ferroelectricity in HZO films.[33] The existence of the non-ferroelectric tetragonal phase is not detrimental since the ferroelectric behavior was evidenced in HZO films, where the tetragonal and orthorhombic phases co-existed.[34]

Figure 4(a) also shows that both the diffraction peaks related to the orthorhombic and tetragonal phases pop up at 370 °C, which likely represents the start of film crystallization. At this temperature, the HZO crystallite formation process with the metastable

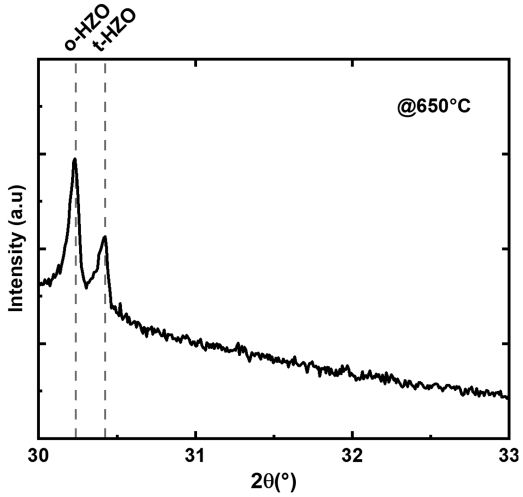

FIG. 5. XRD pattern of the TiN/22 nm-thick HZO/TiN stack annealed at 650 °C under a nitrogen atmosphere.

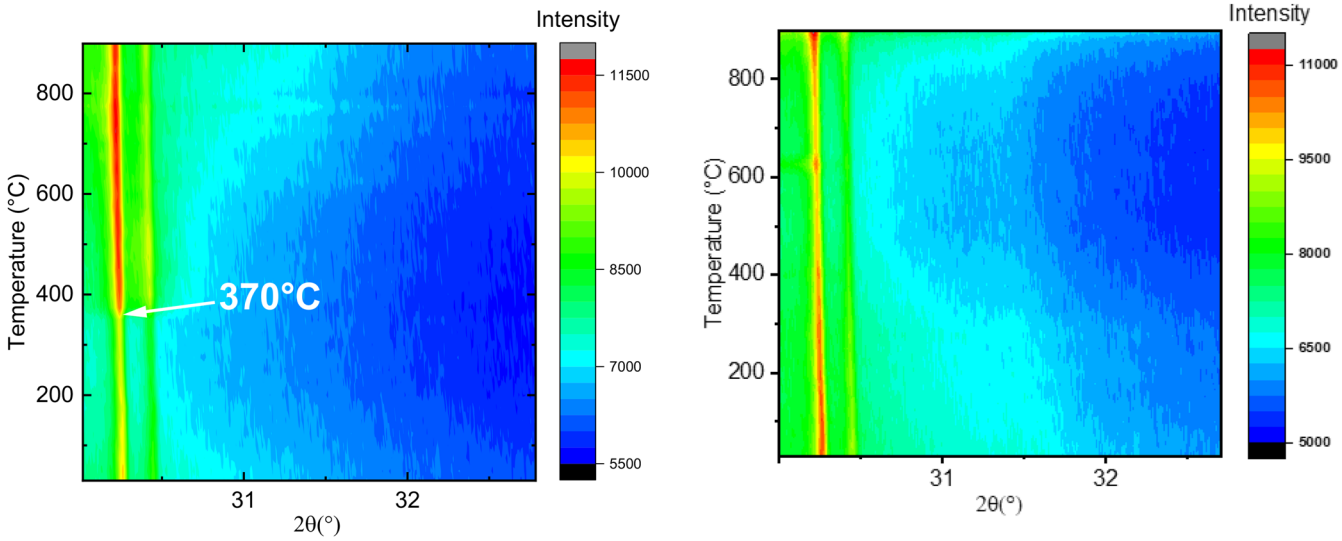

FIG. 4. XRD patterns of the TiN/22 nm-thick HZO/TiN stack at different *in situ* thermal annealing temperatures in the range of 30–900 °C under a nitrogen atmosphere during (a) heating and (b) cooling down.

© Author(s) 2021

orthorhombic/tetragonal phases begins. However, the Curie temperature of ferroelectric HfO_2 is believed to be in the range of 400–500 °C.[15] The onset of the crystallization of the orthorhombic phase at lower temperature might be explained by the presence of Zr since ZrO_2 has a lower Curie temperature.[28] As the annealing temperature increases beyond 370 °C, the intensity of both peaks remains stable up to 900 °C, suggesting that no transition to the monoclinic phase occurs.

Figure 4(b) shows the evolution of the XRD pattern during cooling down of the TiN/22 nm-thick HZO/TiN stack from 900 °C to room temperature. It can be seen that the two diffraction peaks related to the orthorhombic and tetragonal phases persist down to room temperature with only a small decrease in intensity. This stability suggests that the orthorhombic phase does not disappear during cooling down and that no phase transition to the monoclinic phase is observed.

In summary, the *in situ* XRD analysis of the crystallization process of the 22 nm-thick HZO film upon thermal annealing under a nitrogen atmosphere exhibits three interesting results. First, the amorphous HZO film starts to crystallize in the orthorhombic/tetragonal phases at a low annealing temperature of 370 °C. The intensities of the corresponding diffraction peaks do not show any noticeable increase up to 900 °C. Second, the orthorhombic related diffraction peak persists during the cooling down to room temperature. Third, the crystallization of HZO films in the orthorhombic phase can be achieved through a standard thermal annealing process, whereas most of the results reported on the crystallization of HfO_2-based materials show that rapid thermal annealing[23,35,36] must be used in order to stabilize the orthorhombic phase.

Finally, TEM analysis was performed on the TiN/22 nm-thick HZO/TiN stack annealed at 650 °C in order to get an insight into the crystallinity of the HZO film and its interfaces with the TiN. Figure 6 shows a highly uniform HZO film with no inter-layers between the HZO and TiN electrodes. Moreover, the formation of crystallites with a typical diameter of about 10 nm is observed.

C. Electrical characterizations

1. Current–voltage characteristics

In this section, I–V characteristics were determined on the TiN/HZO/TiN stacks to ensure the absence of important leakage current that might hinder the observation of HZO film ferroelectric behavior. Indeed, high leakage current can prevent the buildup of electric field across the Metal-Insulator-Metal (MIM) structure, resulting in very poor dielectric polarization of the HZO layer. In addition, it was shown that the leakage current density across HZO layers is strongly influenced by the process conditions.[37] Hence, in this work, I–V characteristics were used to screen the leaky devices across the sample batch that was fabricated.

Figure 7 shows the I–V characteristic of the TiN/HZO (14 nm)/TiN stack annealed at 650 °C for 1 min. It shows a current density of ~2×10^{-7} A/cm^2 at 0.7 V, which is in accordance with the reported values for sputtered HZO[23,38] and even better than the values obtained on co-sputtered HZO annealed under N_2.[23] The annealing at 650 °C showed the best values of leakage current compared to the other annealing temperature used in this study. We believe that these superior electrical results are due to the enhanced density of the HZO films, thanks to the high power applied to the HZO target (400 W) during film deposition.[39] An additional annealing of HZO films under an oxygen atmosphere could reduce the leakage current by reducing the number of defects within the films.[23]

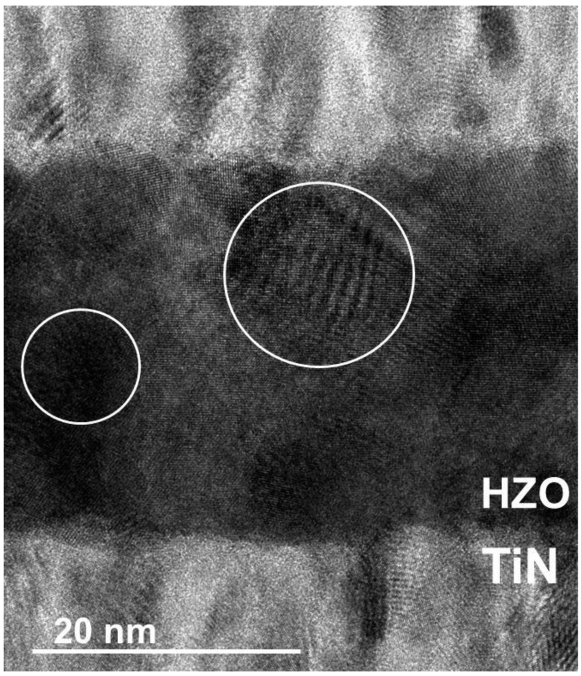

FIG. 6. TEM image of the TiN/22 nm-thick HZO/TiN stack evidencing crystallites with ~10 nm diameter.

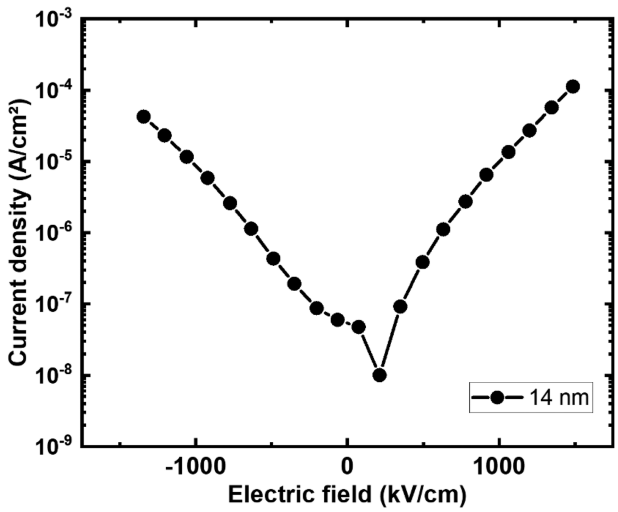

FIG. 7. Current–voltage characteristic of the TiN/HZO(14 nm)/TiN stack annealed at 650 °C for 1 min.

© Author(s) 2021

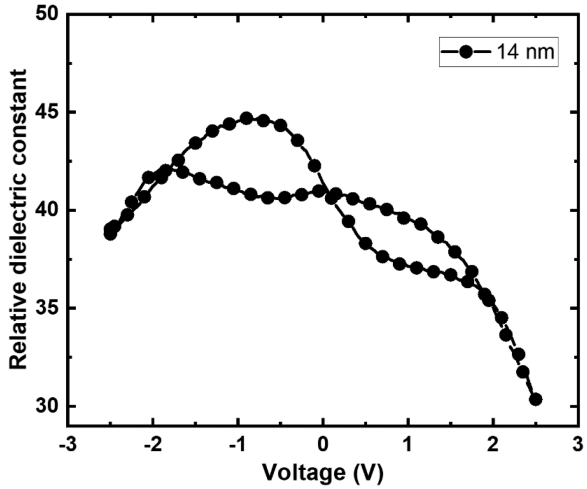

FIG. 8. Relative dielectric constant vs voltage for TiN/HZO(14 nm)/TiN stack annealed during 1 min at 650 °C under N2.

IV. CAPACITANCE–VOLTAGE CHARACTERISTICS

C–V characteristics were determined on the Ti/HZO (14 nm)/TiN stacks, which showed an orthorhombic HZO phase in order to investigate the ferroelectric behavior of the HZO layer. Indeed, besides the well-known polarization–electric field hysteresis (P–E) plot, the so-called butterfly-shaped C–V plot is also used to evidence the ferroelectric behavior.[7,21,23,24,28] Figure 8 shows the dielectric constant vs voltage plot extracted from the experimental C–V data of the 14 nm-thick HZO layer. A butterfly-shaped C–V plot usually attributed to the ferroelectric polarization is obtained at positive and negative polarization once the coercive field is reached. This result is consistent with the structural analysis obtained in the previous sections. Indeed, the butterfly shape shown in Fig. 8 is correlated with the occurrence of the orthorhombic/tetragonal phases after the annealing of the TiN/HZO/TiN stack at 650 °C. The values of the dielectric constant ε_r in the range of 30–45 are in agreement with the published data for HZO layers obtained by ALD or sputtering.[21,40]

However, it is noteworthy that the obtained dielectric constants of the single-target sputtered HZO are somewhat higher than those reported for co-sputtering HZO layers. This can be related to the difference in the fraction of tetragonal and orthorhombic phases. Indeed, the dielectric constant of the HZO tetragonal phase is 70,[30] whereas that of the orthorhombic phase is 40.[28,29]

V. CONCLUSION

In this work, the chemical composition and structural and electrical properties of HZO single target sputtered thin films were studied in order to investigate their ferroelectric behavior. First, XPS analysis showed the same chemical composition of the deposited HZO in different conditions, which represents a major advent of the single-target sputtering combined with a high deposition rate. Second, the structural signature of ferroelectric HZO, i.e., the orthorhombic/tetragonal phase, was evidenced by GIXRD on HZO films exposed to rapid thermal annealing and, more interestingly, also on HZO films exposed to slow and dynamic thermal annealing at temperatures ramped from 370 to 900 °C under a N_2 atmosphere. Indeed, *in situ* XRD analysis performed during the increase in temperature showed the apparition of the HZO orthorhombic phase at 370 °C that persisted up to 900 °C and also during cooling down to room temperature. Third, the low leakage current density obtained for 14 nm thick HZO confirmed the good electric nature of the films, which is a prerequisite to ferroelectricity. Finally, capacitance–voltage cycles showed butterfly-shaped curves, which gives a strong indication of the ferroelectric behavior and which is consistent with the structural analysis that evidenced the HZO orthorhombic phase.

ACKNOWLEDGMENTS

This work was supported by the French National Research Agency in the framework of the "Investissements d'Avenir" Program (Grant No. ANR-15-IDEX-02) through the Cross Disciplinary Project NEED and by Renatech, a French national nanofabrication network. M.B.H. held a doctoral fellowship from the project CDP NEED.

DATA AVAILABILITY

The data that support the findings of this study are available from the corresponding authors upon reasonable request.

REFERENCES

[1] E. Defaÿ, T. Lacrevaz, T. T. Vo, V. Sbrugnera, C. Bermond, M. Aïd, and B. Fléchet, Appl. Phys. Lett. **94**, 052901 (2014).
[2] S. Tadigadapa and K. Mateti, Meas. Sci. Technol. **20**, 092001 (2009).
[3] K. H. Koh, T. Kobayashi, and C. Lee, Sens. Actuators, A **184**, 149 (2012).
[4] C. Shi, J. Ma, J. Wu, X. Wang, F. Miao, Y. Huang, K. Chen, W. Wu, and B. Wu, J. Alloys Compd. **846**, 156245 (2020).
[5] G. Clementi, G. Lombardi, S. Margueron, M. A. Suarez, E. Lebrasseur, S. Ballandras, J. Imbaud, F. Lardet-Vieudrin, L. Gauthier-Manuel, B. Dulmet, M. Lallart, and A. Bartasyte, Mech. Syst. Signal Process. **149**, 107171 (2021).
[6] Y. Wang, C. Luo, S. Wang, C. Chen, G. Yuan, H. Luo, and D. Viehland, Adv. Electron. Mater. **6**, 1900949 (2020).
[7] T. S. Böscke, J. Müller, D. Bräuhaus, U. Schröder, and U. Böttger, Appl. Phys. Lett. **99**, 102903 (2011).
[8] T. Ali, P. Polakowski, S. Riedel, T. Buttner, T. Kampfe, M. Rudolph, B. Patzold, K. Seidel, D. Lohr, R. Hoffmann, M. Czernohorsky, K. Kuhnel, P. Steinke, J. Calvo, K. Zimmermann, and J. Muller, IEEE Trans. Electron Devices **65**, 3769 (2018).
[9] D.-H. Min, S.-E. Moon, and S.-M. Yoon, J. Phys. D: Appl. Phys. **53**, 115109 (2020).
[10] T. Mikolajick, S. Slesazeck, M. H. Park, and U. Schroeder, MRS Bull. **43**, 340 (2018).
[11] M. Li, X. Yin, X. S. Hu, and C. Zhuo, in *2020 25th Asia and South Pacific Design Automation Conference (ASP-DAC)* (IEEE, Beijing, China, 2020), pp. 562–567.
[12] Y. Goh and S. Jeon, Nanotechnology **29**, 335201 (2018).
[13] A. Dörfler, G. Kolhatkar, U. Wagner, and A. Ruediger, J. Phys.: Condens. Matter **32**, 185302 (2020).
[14] F. Mehmood, T. Mikolajick, and U. Schroeder, Appl. Phys. Lett. **117**, 092902 (2020).
[15] T. Shimizu, K. Katayama, T. Kiguchi, A. Akama, T. J. Konno, O. Sakata, and H. Funakubo, Sci. Rep. **6**, 32931 (2016).
[16] S. Mueller, C. Adelmann, A. Singh, S. Van Elshocht, U. Schroeder, and T. Mikolajick, ECS J. Solid State Sci. Technol. **1**, N123 (2012).
[17] A. Wei, C. Chen, L. Tang, K. Zhou, and D. Zhang, J. Alloys Compd. **731**, 546 (2018).

© Author(s) 2021

[18]J. Müller, T. S. Böscke, D. Bräuhaus, U. Schröder, U. Böttger, J. Sundqvist, P. Kücher, T. Mikolajick, and L. Frey, Appl. Phys. Lett. **99**, 112901 (2011).
[19]S. Starschich and U. Boettger, J. Mater. Chem. C **5**, 333 (2017).
[20]K. Chae, J. Hwang, E. Chagarov, A. Kummel, and K. Cho, J. Appl. Phys. **128**, 054101 (2020).
[21]T.-H. Ryu, D.-H. Min, and S.-M. Yoon, J. Appl. Phys. **128**, 074102 (2020).
[22]J. Woo, Y. Goh, S. Im, J. H. Hwang, Y. Kim, J. H. Kim, J.-P. Im, S.-M. Yoon, S. E. Moon, and S. Jeon, IEEE Electron Device Lett. **41**, 232 (2020).
[23]Y. H. Lee, H. J. Kim, T. Moon, K. D. Kim, S. D. Hyun, H. W. Park, Y. B. Lee, M. H. Park, and C. S. Hwang, Nanotechnology **28**, 305703 (2017).
[24]L. Xu, T. Nishimura, S. Shibayama, T. Yajima, S. Migita, and A. Toriumi, J. Appl. Phys. **122**, 124104 (2017).
[25]S. J. Lee, M. J. Kim, T. Y. Lee, T. I. Lee, J. H. Bong, S. W. Shin, S. H. Kim, W. S. Hwang, and B. J. Cho, AIP Adv. **9**, 125020 (2019).
[26]S. U. Sharath, T. Bertaud, J. Kurian, E. Hildebrandt, C. Walczyk, P. Calka, P. Zaumseil, M. Sowinska, D. Walczyk, A. Gloskovskii, T. Schroeder, and L. Alff, Appl. Phys. Lett. **104**, 063502 (2014).
[27]D. Sotiropoulou and S. Ladas, Surf. Sci. **408**, 182 (1998).
[28]J. Müller, T. S. Böscke, U. Schröder, S. Mueller, D. Bräuhaus, U. Böttger, L. Frey, and T. Mikolajick, Nano Lett. **12**, 4318 (2012).
[29]R. Alcala, C. Richter, M. Materano, P. D. Lomenzo, C. Zhou, J. L. Jones, T. Mikolajick, and U. Schroeder, J. Phys. D: Appl. Phys. **54**, 035102 (2021).
[30]R. Materlik, C. Künneth, and A. Kersch, J. Appl. Phys. **117**, 134109 (2015).
[31]M. Dogan, N. Gong, T.-P. Ma, and S. Ismail-Beigi, Phys. Chem. Chem. Phys. **21**, 12150 (2019).
[32]M. H. Park, T. Schenk, C. M. Fancher, E. D. Grimley, C. Zhou, C. Richter, J. M. LeBeau, J. L. Jones, T. Mikolajick, and U. Schroeder, J. Mater. Chem. C **5**, 4677 (2017).
[33]M. H. Park, H. J. Kim, Y. J. Kim, W. Lee, T. Moon, and C. S. Hwang, Appl. Phys. Lett. **102**, 242905 (2013).
[34]D. H. Triyoso, R. D. Clark, S. Consiglio, K. Tapily, H. Higuchi, T. Hakamata, D. Newman, S. Rogalskyj, C. Cole, A. Raley, C. Wajda, and G. Leusink, in *2020 4th IEEE Electron Devices Technology and Manufacturing Conference (EDTM)* (IEEE, Penang, Malaysia, 2020), pp. 1–4.
[35]T. Kim, J. Park, B.-H. Cheong, and S. Jeon, Appl. Phys. Lett. **112**, 092906 (2018).
[36]J. Bouaziz, P. Rojo Romeo, N. Baboux, R. Negrea, L. Pintilie, and B. Vilquin, APL Mater. **7**, 081109 (2019).
[37]R. I. Damir, A. G. Chernikova, and M. G. Kozodaev, J. Phys.: Conf. Ser. **864**, 011001 (2017).
[38]J. Bouaziz, P. Rojo Romeo, N. Baboux, and B. Vilquin, J. Vac. Sci. Technol. B **37**, 021203 (2019).
[39]Y. Kouzuma, K. Teii, K. Uchino, and K. Muraoka, Phys. Rev. B **68**, 064104 (2003).
[40]T. Kim, M. An, and S. Jeon, AIP Adv. **10**, 015104 (2020).

© Author(s) 2021